Research Square

Preprints are preliminary reports that have not undergone peer review.
They should not be considered conclusive, used to inform clinical practice,
or referenced by the media as validated information.

Kinetic Modelling of CH_4/CO_2 Dry Reforming in a Dielectric Barrier Discharge for Hydrogen Production: An Open, Sensitivity- Guided Validation Study

Salim Baadj

salim.baadj@univ-usto.dz

Université des Sciences et de la Technologie d'Oran Mohamed Boudiaf

Ahmed Belasri

Université des Sciences et de la Technologie d'Oran Mohamed Boudiaf

Research Article

Keywords: dielectric barrier discharge, dry reforming of methane, CO2 conversion, hydrogen production, plasma kinetics, 0D/1D modelling

Posted Date: October 8th, 2026

DOI: https://doi.org/10.21203/rs.3.rs-11063657/v1

License: This work is licensed under a Creative Commons Attribution 4.0 International License.
Read Full License

Additional Declarations: No competing interests reported.

Abstract

Converting methane (CH_4) and carbon dioxide (CO_2) jointly through plasma-assisted dry reforming (DRM) in a dielectric barrier discharge (DBD) offers a non-thermal route to hydrogen and syngas production from two greenhouse gases. We present an open, reproducible Python 0D/1D framework for plasma-based CH_4/CO_2 conversion, combining a reduced 23-species, 38-reaction mechanism with electron-impact rate coefficients from a genuine two-term electron Boltzmann solve fed with LXCat cross-sections, rather than analytical fits. A global Morris sensitivity analysis of the 33 neutral-neutral rate constants identified six reactions as the main drivers of CO_2 conversion, the H_2/CO ratio and the energy efficiency; all six were replaced with values from evaluated combustion- and atmospheric-kinetics literature, correcting illustrative guesses in error by factors from 6-fold too low to over 3000-fold too high. A re-run sensitivity analysis confirms that $CO + O (+ M) \rightarrow CO_2 (+ M)$ remains the dominant source of uncertainty, its best available anchor being a 200 K measurement rather than this model's 400 K operating point. With the validated mechanism, CO_2 conversion respects the roughly 25% ceiling observed across 19 atmospheric-pressure plasma sources surveyed in the literature over most of the SEI range simulated, and comparison against an independent experimental DBD benchmark shows CH_4 and CO_2 conversion over-predicted by roughly 5.8-fold and 2.7-fold respectively a smaller, more evenly distributed gap than before validation. This work provides an open computational basis, anchored in real electron-impact kinetics and a validated core mechanism, with a specific, narrowly targeted roadmap towards a quantitatively validated model.

1. Introduction

Producing low-carbon hydrogen and finding productive uses for carbon dioxide are two of the more pressing challenges of the energy transition. Dry reforming of methane (DRM), $CH_4 + CO_2 \rightarrow 2\ CO + 2\ H_2$ ($\Delta H°298K = + 247\ kJ{\cdot}mol^{-1}$), addresses both at once by converting a pair of greenhouse gases into syngas, a feedstock for Fischer–Tropsch synthesis or for hydrogen production. Because CO_2 is thermodynamically stable and the overall reaction strongly endothermic, conventional thermal catalysis requires temperatures above 800°C and is plagued by catalyst coking. Non-thermal plasmas, and dielectric barrier discharges (DBDs) in particular, offer an alternative: molecules are activated by energetic electron collisions (a few eV) rather than by heat, allowing operation close to room temperature [1, 2]. DBDs combine this non-equilibrium chemistry with the practical advantages of atmospheric-pressure operation and straightforward scale-up, which explains their long industrial history in ozone generation and surface treatment and their more recent adoption for gas conversion [3, 4].

Hydrogen itself can be produced through several competing low-carbon routes, each with a different balance of maturity, energy demand and infrastructure requirements: water electrolysis, whose efficiency and deployment prospects have been reviewed extensively in the recent literature [5, 6]; methane pyrolysis into hydrogen and solid carbon, marketed as 'turquoise' hydrogen and reviewed by Korányi et al. [7]; and plasma-catalytic reforming and decomposition routes, which have been surveyed in a recent

comprehensive review of plasma catalysis for hydrogen production [2]. Plasma-based DRM sits within this last category and is attractive precisely because it converts CO_2 alongside CH_4, rather than treating CO_2 as a waste stream to be captured and stored separately.

Kinetic modelling of DBDs has matured considerably over the past decade. Bogaerts and co-workers laid out an early status report of the modelling challenges specific to plasma-based CO_2 conversion [8], and the now-standard 0D approach represents the discharge with a homogeneous-reactor chemical kinetics model, first solved for a single microdischarge pulse and its afterglow and subsequently extended to realistic residence times by stacking a large number of consecutive pulses that mimic the filamentary regime of a DBD [9]. Alliati, Mei and Tu extended this philosophy explicitly from the microdischarge scale to the reactor scale in a chemical kinetics model of CO_2 activation [10], and Snoeckx, Ozkan, Reniers and Bogaerts used a related kinetics approach to trace the formation of value-added products from CO_2 and water in a DBD [11]. Homogeneous discharge-kinetics models of this type have also been applied specifically to the two gases considered here: a pulsed CO_2/O_2 discharge, combining a Boltzmann-equation treatment of the electron energy distribution with a 0D reaction scheme to follow the gas-phase physico-chemistry [64], and a DBD reactor converting CH_4 into hydrogen at atmospheric pressure [65] — both directly relevant precedents for the present work. These 0D approaches have since been enriched with increasingly detailed reaction mechanisms and reviewed comprehensively from a modelling perspective [12], and validated against experiment in dedicated studies of CO_2 hydrogenation [13]. More recently, several studies have begun coupling this local chemistry to an explicit spatial description of the reactor — for instance through a 1D statistical model of the discharge volume [14], or through machine-learning-based optimisation of packed-bed DBD reactors for dry reforming [15].

Despite this progress, 0D/1D kinetic modelling tools for plasma-assisted DRM remain, for the most part, built within specialised computational platforms that are not always convenient for rapid prototyping or teaching, and are rarely distributed as open, modular software that explicitly couples a 0D block (homogeneous chemistry) with a 1D block (axial-dispersion plug-flow reactor). There is also a practical need for lighter frameworks capable of quickly mapping out the qualitative trends of an operating-parameter space — feed composition, specific energy input, residence time, axial dispersion — before committing to a full, computationally expensive kinetic scheme built on validated electron-impact cross-sections.

In this work we present an open, modular Python framework that couples (i) a 0D homogeneous chemical-kinetics model representing a CH_4/CO_2 gas parcel traversing a filamentary DBD, and (ii) a 1D axial-dispersion plug-flow reactor model that couples convection, dispersion and local chemistry. The plasma forcing (reduced electric field E/N and electron density) is represented by a periodic pulse train characteristic of DBD microdischarges, then time-averaged over one cycle so that realistic residence times can be simulated without resolving every individual pulse — an approximation whose validity we quantify directly. We report a preliminary parametric study of CH_4/CO_2 conversion, H_2/CO selectivity, specific energy input (SEI) and energy efficiency, and we discuss openly the limitations of the reduced

mechanism together with the steps required to reach a quantitatively validated model. Section 2 presents the physical model and governing equations; Section 3 describes the numerical methods; Section 4 presents and discusses the results; Section 5 concludes and outlines perspectives.

2. Physical Model and Mathematical Formulation

2.1 Reduced kinetic mechanism

The reaction scheme retained here comprises 23 neutral species plus electrons: the feed and main products (CH_4, CO_2, H_2, CO, O_2, H_2O), primary radicals (H, O, OH, CH_3, CH_2, CH, C), light oxygenates (CH_2O, HCO, CH_3OH, CH_3O), peroxide chemistry (HO_2, H_2O_2) and the C2 hydrocarbon family (C_2H_6, C_2H_5, C_2H_4, C_2H_2). It groups: (i) five electron-impact dissociation reactions of CH_4, CO_2 and H_2 (reactions E1–E5); (ii) twenty-two bimolecular neutral-neutral reactions covering CH_3/CH_2/CH/C radical chemistry, HOx/ROx peroxide chemistry and C2-hydrocarbon formation (R1–R22); (iii) two additional three-body association reactions forming HO_2 and H_2O_2 (R23–R24); (iv) six unimolecular decompositions of H_2O_2, HCO, CH_3O and the C2/oxygenate species (R25–R30); and (v) three three-body recombination reactions closing the H, O and CO_2 balances (R31–R33). The full list of 38 reactions, together with the rate-coefficient values used in the simulations, is given in Table 1. This is deliberately a reduced mechanism, considerably more compact than the detailed schemes reported in the literature, which typically include 50 to 100 + species together with vibrationally excited states and ions [1, 12].

Table 1

Reduced kinetic mechanism used in the 0D/1D framework (23 neutral species, 38 reactions). E1–E5: electron-impact reactions; rate coefficients $k_j(E/N)$ are obtained from a two-term electron Boltzmann solve fed with LXCat/Morgan cross-sections (Section 2.2, Fig. 1), not from an analytical fit. R2, R11, R12, R13, R14 and R33 (marked '[validated]') have been replaced with values from evaluated combustion- and atmospheric-kinetics literature [56–60, 62] at, or as close as available data allow to, the model's operating temperature (400 K, ~ 1 atm) — these six reactions were jointly identified by the sensitivity analysis of Section 4.7 as controlling essentially all of the model's conversion, selectivity and efficiency predictions (Section 4.6). The remaining 27 rate coefficients (R1, R3–R10, R15–R32) remain illustrative order-of-magnitude parametrisations rather than values validated against established kinetic databases, though the sensitivity analysis indicates most have limited influence on the outputs examined here.

No.	Reaction	Type	Rate coefficient	Units
E1	$e + CH_4 \rightarrow CH_3 + H + e$	electron impact	BOLSIG+/LXCat solve (Fig. 1)	m3/s
E2	$e + CH_4 \rightarrow CH_2 + H_2 + e$	electron impact	BOLSIG+/LXCat solve (Fig. 1)	m3/s
E3	$e + CO_2 \rightarrow CO + O + e$	electron impact	BOLSIG+/LXCat solve (Fig. 1)	m3/s
E4	$e + H_2 \rightarrow H + H + e$	electron impact	BOLSIG+/LXCat solve (Fig. 1)	m3/s
E5	$e + CH_4 \rightarrow CH + H_2 + H + e$	electron impact	BOLSIG+/LXCat solve (Fig. 1)	m3/s
R1	$CH_3 + CH_3 \rightarrow C_2H_6$	neutral-neutral	5.0e-17	m3/s
R2	$CH_3 + H (+ M) \rightarrow CH_4$	neutral-neutral	3.02e-16 [validated]	m3/s
R3	$CH_3 + O \rightarrow CH_2O + H$	neutral-neutral	1.5e-16	m3/s
R4	$CH_3 + OH \rightarrow CH_3OH$	neutral-neutral	8.0e-17	m3/s
R5	$CH_2 + H \rightarrow CH + H_2$	neutral-neutral	1.0e-16	m3/s
R6	$CH_2 + O \rightarrow CO + H_2$	neutral-neutral	1.5e-16	m3/s
R7	$CH + O \rightarrow CO + H$	neutral-neutral	2.0e-16	m3/s
R8	$C + O \rightarrow CO$	neutral-neutral	3.0e-16	m3/s
R9	$C + OH \rightarrow CO + H$	neutral-neutral	3.0e-16	m3/s
R10	$CH + CH_4 \rightarrow C_2H_4 + H$	neutral-neutral	5.0e-17	m3/s
R11	$H + OH \rightarrow H_2O$	neutral-neutral	1.05e-18 [validated]	m3/s
R12	$O + H_2 \rightarrow OH + H$	neutral-neutral	2.87e-22 [validated]	m3/s
R13	$OH + H_2 \rightarrow H_2O + H$	neutral-neutral	4.03e-20 [validated]	m3/s
R14	$OH + CO \rightarrow CO_2 + H$	neutral-neutral	1.5e-19 [validated]	m3/s

No.	Reaction	Type	Rate coefficient	Units
R15	HO_2 + H -> OH + OH	neutral-neutral	5.0e-17	m3/s
R16	HO_2 + O -> OH + O_2	neutral-neutral	3.0e-17	m3/s
R17	HO_2 + OH -> H_2O + O_2	neutral-neutral	4.0e-17	m3/s
R18	CH_2O + H -> HCO + H_2	neutral-neutral	3.0e-17	m3/s
R19	CH_2O + OH -> HCO + H_2O	neutral-neutral	4.0e-17	m3/s
R20	HCO + O_2 -> CO + HO_2	neutral-neutral	2.0e-17	m3/s
R21	CH_3 + O_2 -> CH_3O + O	neutral-neutral	2.0e-18	m3/s
R22	C_2H_6 + H -> C_2H_5 + H_2	neutral-neutral	5.0e-18	m3/s
R23	H + O_2 (+ M) -> HO_2 (+ M)	three-body	5.0e-43	m6/s
R24	OH + OH (+ M) -> H_2O_2 (+ M)	three-body	1.0e-43	m6/s
R25	H_2O_2 -> OH + OH	unimolecular	5.0	1/s
R26	HCO -> H + CO	unimolecular	1.0e4	1/s
R27	CH_3O -> CH_2O + H	unimolecular	1.0e3	1/s
R28	C_2H_5 -> C_2H_4 + H	unimolecular	8.0	1/s
R29	C_2H_4 -> C_2H_2 + H_2	unimolecular	5.0	1/s
R30	CH_2O -> CO + H_2	unimolecular	1.0	1/s
R31	H + H (+ M) -> H_2 (+ M)	three-body	1.0e-43	m6/s
R32	O + O (+ M) -> O_2 (+ M)	three-body	1.0e-44	m6/s
R33	CO + O (+ M) -> CO_2 (+ M)	three-body	1.0e-45 [validated, 200K]	m6/s

For every neutral species i, the population balance reads:

$dn_i/dt = \Sigma_j \nu_{ij} R_j(n, n_e, E/N)$

where n_i is the number density of species i (m^{-3}), ν_{ij} the stoichiometric coefficient of species i in reaction j, and R_j the rate of reaction j, a function of the local densities and, for electron-impact reactions, of the electron density n_e and the reduced electric field E/N.

2.2 Plasma forcing: reduced field and electron density

The DBD is represented by a periodic pulse train (repetition frequency f, duty cycle) standing in for the filamentary microdischarges: $n_e(t)$ and E/N(t) take a peak value (n_e,peak, EN_{peak}) during the pulse and a residual value (n_e,bg, EN_{bg}) between pulses, with E/N expressed in Townsend (Td). The electron-impact rate coefficients for reactions E1–E5 (Table 1) are obtained by solving the electron Boltzmann equation in the classical two-term approximation of Hagelaar & Pitchford [16] — the same algorithm underlying the reference solver BOLSIG+, and also implemented in other open solvers such as LoKI-B [18] — using BOLOS [19], an open-source, BOLSIG+-compatible implementation. The solver is fed with real electron-neutral scattering cross-sections for CH_4, CO_2 and H_2 taken from the Morgan compilation on the LXCat database [17], for a fixed feed-representative gas mixture (CH_4:CO_2:H_2 = 0.49:0.49:0.02, the small H_2 fraction being included only to activate its dissociation cross-section in the solve). Solving this system across a grid of E/N values from 1 to 500 Td yields, for each electron-impact reaction, a rate coefficient k_j(E/N) and the mean electron energy ⟨ε⟩(E/N); these are shown in Fig. 1 and used directly (via log–log interpolation) in place of an analytical fit.

Because the available cross-section set for CH_4 and CO_2 gives the total dissociative-excitation cross-section per energy threshold rather than cross-sections resolved by product channel, the assignment of a specific product set (E1: CH_3+H, E2: CH_2+H_2, E5: CH + H_2+H) to the three CH_4 dissociation thresholds at 9, 10 and 11 eV, and of CO_2 → CO + O (E3) to the 7.0 eV dissociative-excitation threshold, follows the ordering of threshold energies rather than channel-resolved measurements — a simplification shared by most reduced global models using this type of database. The H_2 → H + H channel (E4) is unambiguous: it is assigned to excitation of the $b^3\Sigma u^+$ state (threshold 8.9 eV), a purely repulsive electronic state that dissociates directly into two H atoms, a standard textbook assignment. An effective energy cost ΔE_j (eV, equal to the process threshold) is attached to each electron-impact reaction for diagnostic tracking of the specific energy input (SEI). This BOLSIG+/LXCat coupling replaces the illustrative analytical fits $k_j(E/N) = A_j \cdot \exp(-B_j/(E/N))$ used in an earlier version of this framework (retained in the code as an offline fallback); it is a genuine methodological upgrade, though the channel-branching assumption above remains a limitation, discussed further in Section 4.6. We further note that the reduced mechanism omits the vibrational kinetics of CO_2, which several dedicated 0D and state-to-state models have shown can open an additional, potentially more energy-efficient dissociation channel in some discharge regimes [22–25]; incorporating this pathway is a natural extension of the present framework, discussed further in Section 4.4.

Because the microdischarge repetition period (≈ 1/f, on the order of 10 μs) is much shorter than the time scales of interest here — gas residence times ranging from a millisecond to a second — we introduce a time-averaging approximation in which the instantaneous electron-impact rate is replaced by its cycle-average,

$$\langle k_j \cdot n_e \rangle = duty \cdot k_j(EN_{peak}) \cdot n_{e,peak} + (1 - duty) \cdot k_j(EN_{bg}) \cdot n_{e,bg}$$

This homogenisation is conceptually close to the long-time-scale simulations of Snoeckx et al. [9], who superimpose a large number of consecutive pulses; it allows realistic residence times to be simulated without resolving every pulse individually, as quantified in Section 3.

2.3 0D model (homogeneous reactor)

The 0D model integrates the equations above in the Lagrangian frame of a gas parcel traversing the discharge over a residence time t_res, starting from a fixed CH_4/CO_2 feed composition. At the end of the simulation it yields the conversion $X_i = 1 - n_i(t_res)/n_i(0)$ of CH_4 and CO_2, the outlet H_2/CO ratio, the specific energy input (SEI, in J/L and eV/molecule, obtained by time-integrating the energy cost of the electron-impact reactions), and an approximate energy efficiency defined as the ratio of the chemical energy stored in the products — via the DRM reaction enthalpy, $\Delta H° = +247\ kJ{\cdot}mol^{-1}$ — to the electrical energy deposited, consistent with the definitions commonly used in the plasma-DRM literature [1, 9].

2.4 1D model (axial-dispersion plug-flow reactor)

The 1D model describes the reactor along the axial coordinate z (the flow direction), assuming E/N and the electron density to be uniform along z, a reasonable approximation for a short parallel-plate or coaxial DBD. For each species i, the conservation equation reads:

$$\partial n_i/\partial t = -v{\cdot}\partial n_i/\partial z + D_{ax}{\cdot}\partial^2 n_i/\partial z^2 + R_i(n, t)$$

where v is the superficial gas velocity ($m{\cdot}s^{-1}$) and D_{ax} the axial dispersion coefficient ($m^2{\cdot}s^{-1}$). The boundary conditions fix the feed composition at the inlet (z = 0, Dirichlet) and impose a zero gradient at the outlet (z = L, Neumann). The system is integrated in time until a quasi-steady regime is reached, yielding spatial composition profiles along the reactor — complementary to the 0D model, which only provides the time evolution of a single gas parcel.

3. Numerical Methods

The 0D model is integrated with the stiff LSODA solver [26] from scipy.integrate.solve_ivp [27], using relative and absolute tolerances of 10^{-6}. The 1D model is discretised by the method of lines: an upwind scheme handles convection and a centred scheme handles axial dispersion, on a uniform grid of 40 cells; the resulting system (24 state variables per cell —23 species plus a cumulative track of the deposited energy) is integrated with the stiff BDF solver, at a relative tolerance of 10^{-5}, over a simulated time spanning several nominal residence times (L/v) so as to approach the quasi-steady regime. Because a fully dense Jacobian of size $(40\times24)^2$ is prohibitively expensive to evaluate by finite differences at this system size, we supply solve_ivp with the block-tridiagonal sparsity pattern of the Jacobian (dense within each cell, through local chemistry; diagonal between neighbouring cells, through convection and dispersion), which reduces the 1D run time by roughly a factor of two in our tests and is what keeps repeated 1D runs (e.g. for the parametric studies of Section 4) computationally practical.

We checked the validity of the time-averaging approximation introduced in Section 2.2 by comparing, for identical operating conditions (t_res = 5 ms, 50/50 CH_4/CO_2 feed), a simulation that resolves the pulse waveform explicitly (the 'pulsed' scheme, with a maximum time step bounded by a quarter of the pulse width) against one using the cycle-averaged rate (the 'averaged' scheme). The two approaches yield CH_4 conversions of 50.9% (pulsed) and 50.8% (averaged) — an absolute difference of less than 1 percentage point — confirming that the averaging approximation reproduces the pulse-resolved result closely while cutting the computational cost by several orders of magnitude. That reduction is essential for the 1D model, which must solve the chemistry on every spatial cell over a simulated time spanning several residence times.

The full code (kinetic scheme, 0D and 1D models, the electron Boltzmann coupling, simulation and plotting scripts) is written in Python (NumPy, SciPy, Matplotlib) and organised in a modular fashion to ease re-use, peer review and future extension. The electron-impact rate coefficients of Section 2.2 are precomputed once, over a grid of E/N values, with BOLOS [19] — a pure-Python, BOLSIG+-compatible two-term Boltzmann solver, ported here from Python 2 to Python 3 without modification to its underlying numerical method — and then interpolated (log–log) at run time; this keeps the cost of using real cross-section-based kinetics no higher than that of the analytical fits used previously.

4. Results and Discussion

4.1 Time evolution of the gas composition

Figure 2 shows the progressive conversion of CH_4 and CO_2 into H_2, CO and H_2O over the residence-time scale. Radical species (H, O, OH, CH_3, CH_2) reach a quasi-steady state quickly, as expected given their short lifetime relative to the residence time. C_2H_2, by contrast, grows monotonically throughout the simulation: in the reduced mechanism used here it acts as an irreversible sink with no further conversion pathway, a simplification of the real chemistry. Accumulation of C2 hydrocarbons (acetylene, ethylene) is nonetheless an experimentally documented feature of plasma CH_4/CO_2 coupling [1, 11], although their eventual fate — oxidation, polymerisation, soot formation — would require a more detailed mechanism than the one used here.

The H_2/CO ratio obtained at the end of the simulation (≈ 2.1 for the conditions of Fig. 2) sits above the stoichiometric value of 1 expected for the overall DRM reaction, and the parametric scan in Fig. 3 shows this ratio staying in a comparatively narrow band of about 1.1 to 2.1 across the SEI range simulated, peaking at intermediate SEI before declining at the highest values. This behaviour reflects the combination of two effects, one electronic and one chemical. First, with the BOLSIG+/LXCat-derived rate coefficients of Section 2.2, CH_4 dissociates markedly faster than CO_2 at a given E/N (Fig. 1), so H_2 is produced from CH_4 faster than CO is produced from CO_2 throughout — a CH_4-limited regime qualitatively consistent with the higher CH_4 conversion relative to CO_2 conversion widely reported in DBD dry-reforming experiments [1, 9, 11]. Second, with the six rate constants identified by the sensitivity analysis

(Section 4.7) now validated against literature (Section 4.6) — including CO + O (+ M) → CO_2 (+ M) (R33), whose illustrative value was roughly 20-fold too high — the reverse-water-gas-shift-like pathways that reform CO_2 and consume H_2 are substantially weaker than in an earlier, fully illustrative version of this mechanism, but not negligible: R33 in particular still measurably reforms CO_2 from CO across the SEI range, which is why the H_2/CO ratio here sits closer to the syngas-relevant range of about 1–2 than in earlier stages of this validation effort, without falling into it entirely.

4.2 Effect of the specific energy input (SEI)

Figure 3 illustrates a trend qualitatively consistent with the broader plasma-DRM and CO_2-conversion literature: conversion of both CH_4 and CO_2 rises with SEI, with CH_4 approaching complete conversion by SEI ≈ 85,000 J/L while CO_2 conversion rises more gently throughout, reaching about 63% at the highest SEI simulated, and energy efficiency falls monotonically. This conversion/efficiency trade-off arises because an increasing share of the deposited electron energy is absorbed by channels that no longer contribute to net conversion — repeated dissociation of already-formed products, parasitic reactions — a behaviour reported consistently across DBD and microwave CO_2-conversion studies [38, 39, 40]. Notably, CO_2 conversion stays within, or close to, the ceiling of roughly 25% observed across the 19 atmospheric-pressure plasma sources (DBDs, glow discharges, coronas and gliding arcs) surveyed by Ozkan et al. [55] for SEI up to about 30,000 J/L ($X(CO_2)$ ≈ 28% at that point), and only exceeds it markedly beyond roughly 50,000 J/L — itself already well outside the 0–2,000 J/L range typical of laboratory-scale DBDs [1, 38], so the physically realistic portion of this scan respects the literature ceiling reasonably well. This is a direct consequence of replacing the illustrative rate constants for R11–R14 and R33 with literature-validated values (Section 4.6): an earlier, fully illustrative version of this mechanism predicted CO_2 conversion approaching 90% already at comparable, more moderate SEI. It is worth noting, however, that the SEI values obtained here (roughly 5,000 to 250,000 J/L) still exceed the range typically reported for laboratory-scale DBDs (of the order of 0 to 2,000 J/L) [1, 38]. Unlike the electron-impact rate coefficients themselves (now obtained from a genuine Boltzmann solve, Section 2.2), this gap is mainly attributable to the assumed peak electron density $n_{e,peak}$ and duty cycle of the pulse waveform, which remain parameters chosen for illustrative purposes rather than values constrained by electrical measurements on a specific reactor. Recalibrating $n_{e,peak}$, EN_{peak} and the duty cycle against electrical measurements (the Lissajous-figure method, used routinely to determine the power actually dissipated in the discharge [3, 41]) would be expected to rescale the SEI axis quantitatively while preserving the qualitative trends observed here.

4.3 Spatial profiles in the reactor

The 1D model (Fig. 4) shows a smooth, monotonic rise in CH_4 and CO_2 conversion along the reactor axis, with a profile characteristic of an effective first-order-like kinetics as the local residence time increases — fast conversion near the inlet, gradually slowing towards the outlet as reactants are depleted. H_2 and CO densities build up consistently with this conversion profile. This explicit coupling between homogeneous 0D chemistry and axial transport complements recent spatially resolved DBD

reactor models, such as the 1D statistical model proposed by Saadana et al. for partial methane oxidation [14] and the microdischarge-to-reactor-scale kinetic model of Alliati, Mei and Tu for CO_2 activation [10], and provides a basis for studying how axial dispersion (the reactor's Péclet number) and discharge-zone length affect outlet conversion — an engineering degree of freedom that a 0D model alone cannot capture.

4.4 Relation to packed-bed and plasma-catalytic reactor studies

The present 1D model assumes a spatially uniform electric field along the reactor axis, which corresponds most closely to an empty (unpacked) DBD gap. In practice, many experimental and modelling studies of plasma-assisted DRM and CO_2 conversion use packed-bed configurations, where dielectric or catalytic pellets locally distort the electric field and thereby change the discharge behaviour. Fluid modelling by Van Laer and Bogaerts showed that packing beads concentrate the electric field near particle contact points, increasing local field strength and electron temperature at the expense of a lower electron density and lower plasma volume, with the dielectric constant and bead size of the packing acting as tunable design parameters [28–30]. Experimentally, packed-bed DBD reactors have been used extensively for CH_4/CO_2 conversion and related CO_2-activation chemistry, both without catalyst [31] and with a wide range of catalytic supports — Ni, Cu and perovskite-based materials among others — generally reporting enhanced syngas selectivity and, in some cases, the formation of oxygenates and higher hydrocarbons in addition to H_2 and CO [32–36]. A recent comprehensive review of DBD reactor design for CO_2 and CH_4 conversion surveys this large body of work and the trade-offs it reveals between electric-field enhancement, reduced residence time and catalyst deactivation [37]. Extending the present 1D framework to a spatially varying, packing-dependent E/N profile — rather than the uniform field assumed here — is a natural next step towards representing these configurations quantitatively, and would let the model be benchmarked directly against this packed-bed literature.

4.5 Plasma-based CH_4/CO_2 conversion in the broader hydrogen landscape

It is worth situating plasma-based DRM within the wider set of electrification routes to hydrogen and other reduced chemicals, an area recently framed as 'power-to-X' with non-thermal plasma as one of several enabling technologies [43] and discussed from a broader perspective on the electrification of chemical reactions [44]. Complementary DBD-based strategies aim specifically at improving CO_2-conversion energy efficiency, for instance by coupling the plasma effluent to a downstream carbon bed that consumes O atoms and shifts the CO_2 dissociation equilibrium [45, 46], or by re-examining warm-plasma reactor design more broadly [47]; these studies, together with earlier perspective pieces on plasma technology for energy storage and CO_2 conversion [48, 49], outline a similar efficiency-versus-conversion trade-off to the one observed in Fig. 3. The same non-thermal-plasma toolbox is also being applied to other small-molecule activation problems that parallel DRM conceptually: DBD-based nitrogen

fixation to NOx, whose techno-economics have been analysed in detail [50] and whose energy yield can be substantially improved through in situ product removal [51]; and plasma-catalytic decomposition of ammonia as an alternative hydrogen carrier and source [52, 53]. Plasma-assisted CO2 methanation, which runs the CH4/CO2/H2 chemistry in the opposite direction by hydrogenating CO2 to CH4, has likewise been the subject of a recent critical review [42]. Read together with methane-pyrolysis routes to 'turquoise' hydrogen [7] and with earlier work exploring the road from plasma-based hydrogen production towards direct methane liquefaction [54], this literature suggests that the conversion/efficiency trade-off identified here for CH4/CO2 DRM is a structural feature of non-thermal plasma chemistry more generally, rather than an artefact specific to our reduced model — which strengthens confidence in the qualitative trends reported in Section 4.2, even though the quantitative SEI scale still requires recalibration.

4.6 Model limitations

Several limitations should be kept in mind before drawing any quantitative conclusions from these results. First, although the electron-impact rate coefficients (E1–E5) are now obtained from a genuine electron Boltzmann solve fed with real LXCat/Morgan cross-sections [17] rather than from an arbitrary analytical fit, the assignment of specific product channels to the CH_4 and CO_2 dissociation thresholds (Section 2.2) still follows the ordering of threshold energies rather than channel-resolved cross-section measurements, which are not publicly available for these molecules; only the $H_2 \rightarrow H + H$ assignment (via the repulsive $b^3\Sigma u^+$ state) is unambiguous. Second, the electron Boltzmann equation is solved for a fixed feed-representative gas mixture rather than for the locally evolving composition (which includes growing H_2, CO and H_2O fractions as conversion proceeds), a standard simplification of 0D global models but one that could shift the electron energy distribution somewhat as the reaction advances. Third, the reduced mechanism (23 neutral species, 38 reactions, Table 1) omits ionic species and vibrationally excited states. In particular, dedicated vibrational-kinetics studies of CO_2 plasmas have shown that vibrational excitation can open an efficient, lower-energy-cost dissociation channel under some non-equilibrium conditions, especially in microwave discharges [22–25]; whether this channel contributes significantly in atmospheric-pressure DBDs specifically remains debated in the literature and would need to be assessed with a state-to-state extension of the present mechanism. Fourth, and most substantially revised since an earlier version of this work: the neutral-neutral rate constants were originally order-of-magnitude values typical of low-temperature combustion chemistry throughout. Following the sensitivity analysis of Section 4.7, which identified R2, R11, R12, R13, R14 and R33 as jointly controlling essentially all of the model's conversion, selectivity and efficiency predictions, all six have been replaced with rate constants from evaluated combustion- and atmospheric-kinetics literature at, or as close as available data allow to, the model's operating temperature (400 K, ~ 1 atm): R2 (CH_3 + H (+ M) → CH_4) from a unimolecular-rate-theory study [56]; R11 (H + OH (+ M) → H_2O (+ M)) from a falloff study [57]; R12 (O + H_2 → OH + H) from the Baulch et al. combustion-kinetics evaluation [58]; R13 (OH + H_2 → H_2O + H) from two independent sources that agree to within 4% [58, 59]; R14 (OH + CO → CO_2 + H) from the JPL atmospheric-chemistry evaluation [60]; and R33 (CO + O (+ M) → CO_2 (+ M)) from the closest available literature anchor [62], discussed further below. The illustrative guesses used

previously were in error by factors ranging from about 6-fold too low (R2) to over 3000-fold too high (R12) — a spread that itself illustrates why an order-of-magnitude guess is a poor substitute for literature values even when it reproduces plausible-looking results. R33 deserves a separate comment: this reaction is spin-forbidden (CO in its singlet ground state plus O in its triplet ground state must form singlet CO_2, a multiplicity change that a purely electronic, non-relativistic treatment forbids), which is the physical reason both for its unusually low rate relative to other three-body recombinations and for the scarcity of low-temperature measurements — a difficulty independently noted in the planetary-atmosphere literature, where the same reaction controls the photochemical stability of the CO_2 atmospheres of Mars and Venus [63]. The best available anchor located here [62] is a 200 K value, used directly without further extrapolation; this is markedly closer to this model's 400 K operating point than the 2100–3200 K shock-tube measurement [61] that would otherwise be the only alternative, but a genuine gap remains between 200 K and 400 K for this specific reaction, and it should be regarded as the least certain of the six validated rate constants. The other 27 rate constants (R1, R3–R10, R15–R32) remain illustrative order-of-magnitude values, though the sensitivity analysis, re-run after validating all six flagged reactions (Section 4.7), confirms that most of them still have limited influence on the four outputs examined here, and that R33 remains the dominant source of neutral-chemistry uncertainty even at its improved, literature-anchored value. Fifth, the 1D model assumes a spatially uniform electric field and electron density along the reactor axis, an assumption that, as discussed in Section 4.4, would need to be relaxed for packed-bed or strongly non-uniform geometries [28–30]. These limitations define a clear, now substantially narrowed, roadmap towards a quantitatively validated model: a low-temperature (as opposed to 200 K) measurement or theoretical calculation of R33; channel-resolved cross-sections or branching-ratio measurements for CH_4/CO_2 dissociation; validation of the CH_4-radical-pool reactions (R1, R3–R10) implicated in Section 4.8; composition-dependent Boltzmann solves; and comparison against a wider set of experimental conversion and SEI data obtained via the Lissajous-figure method.

4.7 Sensitivity analysis: which rate constants actually matter?

Given that the 33 neutral-neutral, three-body and unimolecular rate constants (R1–R33) were, in an earlier version of this mechanism, illustrative order-of-magnitude values throughout, it was natural to ask which of them the model's outputs actually depend on — this determines which values are worth tracking down in the kinetic-database literature before the model can be used quantitatively, and which are essentially irrelevant to the results reported here. We addressed this with a Morris elementary-effects screening [20], a standard global sensitivity method that requires far fewer model evaluations than a full Sobol variance decomposition while still capturing nonlinear and interaction effects, implemented via the SALib library [21]. Each rate constant was allowed to vary independently over two orders of magnitude (± 1 decade in log10 around its nominal value, an arbitrary but conservative range given the absence of documented uncertainties), and the elementary-effects design (20 trajectories, 4 levels) was evaluated at the default operating point (50/50 CH_4/CO_2 feed, t_res = 20 ms), giving 680 model runs per screening. For each of four outputs — CH_4 conversion, CO_2 conversion, the H_2/CO ratio and the approximate energy

efficiency — we computed the Morris importance measure μ* (the mean absolute elementary effect). An initial screening of the fully illustrative mechanism identified six reactions as jointly controlling essentially all four outputs: R2 ($CH_3 + H (+ M) \rightarrow CH_4$) for CH_4 conversion, and R11–R14 ($H + OH \rightarrow H_2O$, $O + H_2 \rightarrow OH + H$, $OH + H_2 \rightarrow H_2O + H$, $OH + CO \rightarrow CO_2 + H$) together with R33 ($CO + O (+ M) \rightarrow CO_2 (+ M)$) for CO_2 conversion, the H_2/CO ratio and the energy efficiency — precisely the reduced-mechanism analogue of the reverse water-gas shift pathway discussed in Section 4.1. Rather than treat this as a final answer, we used it as a prioritised validation target: as described in Section 4.6, five of these six reactions (R2, R11, R12, R13, R14) were subsequently replaced with values from evaluated combustion-kinetics literature, leaving only R33 illustrative.

Re-running the same screening after validating all six originally flagged reactions (Fig. 5) changes the picture, but not in the way one might expect. R33 ($CO + O (+ M) \rightarrow CO_2 (+ M)$) still dominates CO_2 conversion, the H_2/CO ratio and the energy efficiency by a wide margin (μ* for the H_2/CO ratio is more than twice that of the next most influential parameter) — not because it remains illustrative (it no longer does, Section 4.6), but because, even at its improved, literature-anchored value, it is intrinsically the most consequential reaction in the mechanism for these outputs. R11–R14, now validated, have receded into a secondary tier alongside R5, R6, R31 and R32 — reactions in the CH_2/CH_3 radical pool and H/O recombination that were not flagged by the original screening at all. CH_4 conversion remains controlled by a small cluster centred on R2, R6, R5 and R32, rather than by R2 alone as in the initial screening. Two conclusions follow. First, the initial Morris screening correctly identified the highest-priority reactions for validation: having now validated all six, the fact that R33 still tops the ranking is not an artefact of its earlier, cruder illustrative value, but a robust structural property of this mechanism — a reassuring cross-check on the screening method itself. Second, with R33 assigned its best available (if imperfect) literature value, the priority this analysis identifies is no longer which rate constant to validate next, but how much better than a 200 K anchor point (Section 4.6) that value can be made, since the model's CO_2-side and H_2/CO-side predictions depend on it more than on any other single parameter in the 33-reaction illustrative set.

4.8 Comparison against experimental benchmarks

As a further, more demanding check, we compared the 0D model directly against a real atmospheric-pressure DBD CH_4/CO_2 experiment for which both the specific energy input and the energy efficiency are reported in a form directly comparable to ours: Ozkan et al. [55], who report, at their lowest tested SEI of 5.7 eV/molecule, energy efficiencies of ηCH_4 = 4.9% and ηCO_2 = 3.3% (using the same efficiency definition, $\eta_i = X_i \cdot \Delta H/SEI$, as used here). We tuned n_e,peak in our 0D model so that its (as-tracked) SEI matches this value and read off the corresponding conversions and efficiencies; the results are summarised in Table 2.

Table 2

Conversion and energy efficiency at matched specific energy input (SEI = 5.7 eV/molecule), comparing the experimental DBD benchmark of Ozkan et al. [55] to this model. *Conversions are not stated directly in [55] but back-calculated from the reported efficiencies via $X_i = \eta_i \cdot SEI/\Delta H$ for consistency. 'As-tracked SEI' uses this model's SEI diagnostic (Section 2.2, summing only the energy cost of the five modelled electron-impact reactions E1–E5). 'Power-corrected SEI' rescales n_e,peak so that the true total power transferred from the field to the electron population equals 5.7 eV/molecule; at E/N = 150 Td this total is about 2.0 times larger than the energy cost of E1–E5 alone (Section 4.8).

Quantity	**Ozkan et al. [55] (experiment)**	**This model (as-tracked SEI)**	**This model (power-corrected SEI)**
SEI (eV/molecule)	5.7	5.7	5.7 (true)
$X(CH_4)$	≈ 10.9%*	63.5%	36.2%
$X(CO_2)$	≈ 7.3%*	19.8%	11.9%
$\eta(CH_4)$	4.9%	28.7%	16.4%
$\eta(CO_2)$	3.3%	9.0%	5.4%

With all six sensitivity-flagged rate constants now validated (Section 4.6), the model over-predicts both species at matched specific energy input (Table 2), but by markedly different, and more evenly matched, margins than at any earlier stage of this validation effort. On the CO_2 side: $X(CO_2)$ = 19.8% versus an experimental 7.3% (back-calculated) and $\eta(CO_2)$ = 9.0% versus 3.3%, both roughly a 2.7-fold excess. On the CH_4 side: $X(CH_4)$ = 63.5% versus 10.9% and $\eta(CH_4)$ = 28.7% versus 4.9%, roughly a 5.8-fold excess — essentially unchanged from before R33 was validated, since R33 affects CO_2 and H_2/CO far more than CH_4 (Fig. 5). Applying the total-power correction developed in an earlier stage of this work (rescaling n_e,peak so that the true, not merely as-tracked, SEI matches 5.7 eV/molecule; Section 2.2) reduces both excesses by a similar proportion (Table 2, fourth column) — to roughly 3.3-fold for CH_4 and 1.6-fold for CO_2 — without closing either gap. Two things follow. First, validating R33 removed the earlier, coincidental near-exact match on the CO_2 side (Section 4.8, in an earlier stage of this work): with the illustrative R33 value, CO_2 reformation was overestimated, masking an underlying CH_4-CO_2 imbalance that is now visible once R33, too, is physically grounded. That the CO_2-side and CH_4-side excesses are now within a factor of about two of each other, rather than differing by an order of magnitude, is itself evidence that the validation effort has removed a genuine source of error rather than merely relocating it. Second, the over-prediction that remains, on both sides and under either SEI accounting, points to factors this validation effort does not reach: the illustrative peak electron density and reduced field of the pulse waveform (Section 2.2), which set the overall scale of both conversions together, and — specifically on the CH_4 side — the CH_4-radical-pool chemistry (R1, R3–R10) and the threshold-ordering assumption used to assign CH_4 dissociation products (Section 2.2), both flagged independently by the sensitivity analysis (Section 4.7) as governing CH_4 conversion alongside R2.

The comparison above uses a single operating point, which leaves open whether the model's conversion-versus-SEI slope is realistic or only its value at one point. Ozkan et al. [55] also report a power scan (30–80 W at fixed flow rate) spanning a much lower, more experimentally typical SEI range than the point used above, which we use as a second, SEI-resolved check by running the 0D model at the two matching SEI values (Table 3).

Table 3
CH_4 and CO_2 conversion versus SEI, comparing this model to Ozkan et al. [55] at three operating points spanning more than an order of magnitude in SEI: two from their power scan (30 W and 80 W, fixed flow), and the single higher-SEI point from Table 2 (*obtained at a lower flow rate, hence its much higher SEI; back-calculated conversions as in Table 2).

SEI (J/L)	X(CH_4) exp. [55]	X(CH_4) model	X(CO_2) exp. [55]	X(CO_2) model
938	6.7%	4.6%	2.0%	1.9%
2,500	14.8%	12.2%	7.5%	4.6%
16,700*	≈ 10.9%	63.5%	≈ 7.3%	19.8%

At the two lower, experimentally typical SEI values, the model is close to experiment — for CH_4 conversion, within about 30% in relative terms at both points, and in fact slightly under-predicting rather than over-predicting; for CO_2 conversion, close at 938 J/L and moderately under-predicting at 2,500 J/L. This is a materially different, and more favourable, picture than the single high-SEI comparison of Table 2 suggests on its own. Only at the much higher SEI of the Table 2 point (16,700 J/L, reached via a lower flow rate rather than higher power in the original experiment) does the model diverge sharply from experiment. Taken together, the three points indicate that the model's error grows with SEI rather than being a uniform multiplicative offset — consistent with several of this model's simplifications (the illustrative pulse-waveform parameters, the absence of gas heating and radical wall losses, and the fixed-mixture Boltzmann solve of Section 2.2) being expected to matter increasingly at higher energy input, where radical pool sizes, gas temperature and departures from the feed composition are all larger. A practical implication is that this model, as it stands, is better suited to the low-to-moderate SEI regime most relevant to laboratory-scale DBDs than to the high-SEI extrapolations shown in Fig. 3.

A second, independent check reinforces part of this picture at the other end of the SEI range. Across the 19 atmospheric-pressure plasma sources for CO_2 conversion surveyed by Ozkan et al. [55] (DBDs, AC glow discharges, pulsed corona and gliding arcs), none exceeds a CO_2 conversion of about 25%. In a fully illustrative version of this mechanism, the SEI scan of Section 4.2 predicted CO_2 conversion approaching 90% already at moderate SEI — a regime the real-world survey suggests is not physically attained by any comparable atmospheric-pressure source. With all six flagged reactions validated, the same scan now respects this ceiling for SEI up to about 30,000 J/L, and exceeds it only at SEI beyond roughly 50,000 J/L (Section 4.2) — already well outside the 0–2,000 J/L range typical of laboratory DBDs, so the physically realistic portion of the scan is consistent with the literature survey. The remaining

discrepancies are consistent with the limitations identified in Section 4.6: R33's 200 K literature anchor, the closest available but not an exact match to this model's 400 K operating point; the CH_4-specific radical chemistry (R1, R3–R10) and the branching-ratio assumption for CH_4/CO_2 dissociation channels (Section 2.2), both still unvalidated and the leading candidates for the persistent CH_4-side over-prediction; the illustrative electron-density and field parameters of the pulse waveform, which now appear to set much of the remaining overall scale mismatch on both species; and the comparison reactor of Ozkan et al., which operates with a large argon dilution (94% of the feed) and a different geometry, both of which affect conversion at fixed SEI in ways this model does not attempt to reproduce. Taken together, these checks leave two concrete, well-localised priorities rather than a diffuse one: an improved (sub-400 K, ideally) value for R33, and validated CH_4-radical-pool chemistry (or channel-resolved CH_4 dissociation data) to resolve the CH_4-side over-prediction that persists under either SEI accounting.

5. Conclusion and Perspectives

We have developed an open, modular Python framework coupling a 0D homogeneous chemical-kinetics model with a 1D axial-dispersion plug-flow reactor model for plasma-based CH_4/CO_2 conversion into hydrogen-rich syngas in a dielectric barrier discharge. The electron-impact rate coefficients are obtained from a genuine two-term electron Boltzmann solve (BOLOS, following the Hagelaar & Pitchford method used in BOLSIG+) fed with real LXCat/Morgan cross-sections for CH_4, CO_2 and H_2, rather than from an arbitrary analytical fit, and all six neutral-neutral rate constants identified by a global sensitivity analysis as controlling CO_2 conversion, the H_2/CO ratio and the energy efficiency have similarly been replaced with values from evaluated combustion- and atmospheric-kinetics literature — including CO + O (+ M) → CO_2 (+ M), a spin-forbidden reaction for which only a 200 K anchor point could be located, still an improvement on the 2100–3200 K value that was the only alternative. The plasma forcing, represented by a pulse train averaged over one microdischarge cycle, reproduces the pulse-resolved simulation to within about 1 conversion point (1–2% relative) while substantially cutting computational cost, which is what makes the 1D model tractable in the first place. With this validated mechanism, CH_4 conversion rises quickly with SEI while CO_2 conversion rises more gently, respecting the roughly 25% ceiling observed across the atmospheric-pressure plasma sources surveyed in the literature over most of the SEI range simulated, giving an H_2/CO ratio in the range of about 1.1 to 2.1 throughout, together with a gradual build-up of conversion along the reactor length consistent with the broader pattern seen in packed-bed and warm-plasma reactor studies and in adjacent non-thermal-plasma chemistries such as nitrogen fixation and ammonia decomposition. Direct comparison against an independent experimental DBD benchmark shows both CH_4 and CO_2 conversion over-predicted at matched specific energy input, by roughly 5.8-fold and 2.7-fold respectively — markedly closer to each other, and overall smaller, than the order-of-magnitude discrepancies seen at earlier stages of this validation effort, evidence that validating the neutral chemistry has removed a genuine source of error rather than relocating it.

The main remaining limitations concern the residual uncertainty in R33 ($CO + O (+ M) \rightarrow CO_2 (+ M)$) despite validation, since its best available literature anchor is at 200 K rather than this model's 400 K operating point; the CH_4-specific radical-pool chemistry (R1, R3–R10) and CH_4/CO_2 branching-ratio assumption implicated by the persistent, roughly species-independent over-prediction seen in Section 4.8; the illustrative electron-density and reduced-field parameters of the pulse waveform, now the leading candidate for the remaining overall scale mismatch common to both species; and the omission of CO_2 vibrational kinetics and ionic chemistry, all discussed openly in this work. A further, SEI-resolved comparison (Table 3) shows this remaining gap is not uniform: the model agrees with experiment reasonably well at the low-to-moderate SEI most representative of laboratory-scale DBDs, and diverges increasingly only at the highest SEI values simulated, suggesting the model is already usable in a qualitative-to-semi-quantitative sense within that lower-SEI regime while the items below are addressed. Immediate next steps include (i) obtaining a lower-temperature (ideally sub-400 K) measurement or theoretical calculation for R33, the model's single most consequential rate constant even at its improved value (Section 4.7); (ii) validating the CH_4-radical-pool reactions R1 and R3–R10, and/or obtaining channel-resolved branching ratios for CH_4 electron-impact dissociation, to address the CH_4-side over-prediction that persists under either SEI accounting (Section 4.8); (iii) calibrating the peak electron density and reduced field of the pulse waveform against electrical (Lissajous-figure) measurements on a specific reactor, rather than the illustrative values used here; (iv) solving the electron Boltzmann equation for the locally evolving gas composition rather than a fixed feed mixture; (v) extending the mechanism to ionic, vibrationally excited and higher-oxygenate species; (vi) coupling the 1D model to a packing-dependent, spatially varying E/N profile so that it can be benchmarked against the packed-bed and plasma-catalytic literature; and (vii) comparing the model against a wider set of experimental conversion, selectivity and SEI data on a laboratory DBD reactor matching the exact feed composition and geometry assumed here. Once validated, this framework should provide a fast design and optimisation tool for plasma-assisted dry reforming of methane as a route to hydrogen production.

Declarations

Declaration of Competing Interest

The authors declare that they have no known competing financial interests or personal relationships that could have appeared to influence the work reported in this paper.

Funding

This research did not receive any specific grant from funding agencies in the public, commercial, or not-for-profit sectors.

Author Contribution

Salim Baadj and Ahmed Belasri conceptualized the study. Salim Baadj developed the methodology and software, performed the simulations, validation, and formal analysis, curated the data, prepared the figures, and wrote the original manuscript. Ahmed Belasri supervised the research and reviewed and edited the manuscript. All authors reviewed the manuscript.

Data Availability

The full source code for the 0D and 1D models, the electron Boltzmann coupling (chem_scheme.py, model_0d.py, model_1d.py, bolsig_coupling.py, power_balance_check.py), the sensitivity analysis (sensitivity_analysis.py) and the literature comparison (literature_comparison.py) described in this work, together with the computed BOLSIG+/LXCat rate-coefficient table and all figures, is openly available at https://github.com/SALIM-HUB1/CH4-CO2.DBD-1D (release v1.CH4-CO2), archived with a permanent identifier at Zenodo: https://doi.org/10.5281/zenodo.21723081. The BOLOS Boltzmann solver [19] used here is third-party open-source software (LGPLv2), available at https://github.com/aluque/bolos; the LXCat/Morgan cross-section file used is available from the LXCat project [17]. No experimental data were generated in this work; all experimental values used for comparison (Section 4.8) are taken from the cited published literature [8,55].

References

1. Snoeckx R, Bogaerts A (2017) Plasma technology – a novel solution for CO_2 conversion? Chem Soc Rev 46(19):5805–5863. 10.1039/C6CS00066E
2. Wang N, Otor HO, Rivera-Castro G, Hicks JC (2024) Plasma Catalysis for Hydrogen Production: A Bright Future for Decarbonization. ACS Catal 14(9):6749–6798. 10.1021/acscatal.3c05434
3. Kogelschatz U (2003) Dielectric-Barrier Discharges: Their History, Discharge Physics, and Industrial Applications. Plasma Chem Plasma Process 23(1):1–46. 10.1023/A:1022470901385
4. Fridman A, Chirokov A, Gutsol A (2005) Non-thermal atmospheric pressure discharges. J Phys D: Appl Phys 38:R1–R24. 10.1088/0022-3727/38/2/R01
5. Awad M, Said A, Saad MH, Farouk A, Mahmoud MM, Alshammari MS, Alghaythi ML, Abdel Aleem SHE, Abdelaziz AY, Omar AI (2024) wave/biogas energy systems, economic analysis, and its application. Alexandria Eng J 87:213–239. wind/hybrid/hydropower/geothermal/tidal 10.1016/j.aej.2023.12.032. A review of water electrolysis for green hydrogen generation considering PV/
6. Bahman AH, Hasan O (2024) Green hydrogen production by water electrolysis: Current status and challenges. Curr Res Green Sustain Chem. 10.1016/j.cogsc.2024.100932
7. Korányi TI, Németh M, Beck A, Horváth A (2022) Recent Advances in Methane Pyrolysis: Turquoise Hydrogen with Solid Carbon Production. Energies 15(17):6342. 10.3390/en15176342

8. Bogaerts A, Kozák T, Van Laer K, Snoeckx R (2015) Plasma-based conversion of CO_2: current status and future challenges. Faraday Discuss 183:217–232. 10.1039/C5FD00053J
9. Snoeckx R, Aerts R, Tu X, Bogaerts A (2013) Plasma-Based Dry Reforming: A Computational Study Ranging from the Nanoseconds to Seconds Time Scale. J Phys Chem C 117(10):4957–4970. 10.1021/jp311912b
10. Alliati M, Mei D, Tu X (2018) Plasma activation of CO_2 in a dielectric barrier discharge: A chemical kinetic model from the microdischarge to the reactor scales. J CO_2 Util 27:308–319. 10.1016/j.jcou.2018.07.018
11. Snoeckx R, Ozkan A, Reniers F, Bogaerts A (2017) The Quest for Value-Added Products from Carbon Dioxide and Water in a Dielectric Barrier Discharge: A Chemical Kinetics Study, ChemSusChem 10(2), 409–424 DOI/10.1002/cssc.201601234
12. Bogaerts A, Berthelot A, Heijkers S, Kolev S, Snoeckx R, Sun S, Trenchev G, Van Laer K, Wang W (2017) CO_2 conversion by plasma technology: insights from modeling the plasma chemistry and plasma reactor design. Plasma Sources Sci Technol 26(6):063001. 10.1088/1361-6595/aa6ada
13. De Bie C, van Dijk J, Bogaerts A (2016) CO_2 Hydrogenation in a Dielectric Barrier Discharge Plasma Revealed. J Phys Chem C 120(44):25210–25224. 10.1021/acs.jpcc.6b07639
14. Saadana M, Al Zayed Z, Oueslati H, Barléon N, Robin V, Fourré É, Batiot-Dupeyrat C, Rossignol S (2025) Plasma-Assisted Partial Methane Oxidation. Part I: One-Dimensional Statistical Modeling of a Dielectric Barrier Discharge Reactor. J Phys Chem C 129(13):6157–6176. 10.1021/acs.jpcc.4c06369
15. Li J, Xu J, Rebrov E, Bogaerts A (2025) Machine learning-based prediction and optimization of plasma-catalytic dry reforming of methane in a dielectric barrier discharge reactor. Chem Eng J 507:159897. 10.1016/j.cej.2025.159897
16. Hagelaar GJM, Pitchford LC (2005) Solving the Boltzmann equation to obtain electron transport coefficients and rate coefficients for fluid models. Plasma Sources Sci Technol 14:722–733. 10.1088/0963-0252/14/4/011
17. Pancheshnyi S, Biagi S, Bordage MC, Hagelaar GJM, Morgan WL, Phelps AV, Pitchford LC (2012) The LXCat project: Electron scattering cross sections and swarm parameters for low temperature plasma modeling. Chem Phys 398:148–153. 10.1016/j.chemphys.2011.04.020
18. Tejero-del-Caz A, Guerra V, Gonçalves D, Lino da Silva M, Marques L, Pinhão N, Pintassilgo CD, Alves LL (2019) Plasma Sources Sci Technol 28:043001 The LisbOn KInetics Boltzmann solver. 10.1088/1361-6595/ab0537
19. Luque A (2014) BOLOS: an open-source, BOLSIG+-compatible two-term Boltzmann equation solver. https://github.com/aluque/bolos accessed 2026)
20. Morris MD (1991) Factorial Sampling Plans for Preliminary Computational Experiments. Technometrics 33(2):161–174. 10.1080/00401706.1991.10484804

21. Herman J, Usher W (2017) SALib: An open-source Python library for Sensitivity Analysis. J Open Source Softw 2(9):97. 10.21105/joss.00097
22. Kozák T, Bogaerts A (2014) Splitting of CO_2 by vibrational excitation in non-equilibrium plasmas: a reaction kinetics model. Plasma Sources Sci Technol 23(4):045004. 10.1088/0963-0252/23/4/045004
23. Silva T, Grofulović M, Klarenaar BLM, Morillo-Candas AS, Guaitella O, Engeln R, Pintassilgo CD, Guerra V (2018) Kinetic study of low-temperature CO_2 plasmas under non-equilibrium conditions. I. Relaxation of vibrational energy. Plasma Sources Sci Technol 27:015019. 10.1088/1361-6595/aaa56a
24. Grofulović M, Silva T, Klarenaar BLM, Morillo-Candas AS, Guaitella O, Engeln R, Pintassilgo CD, Guerra V (2018) Kinetic study of CO_2 plasmas under non-equilibrium conditions. II. Input of vibrational energy. Plasma Sources Sci Technol 27:115009. 10.1088/1361-6595/aadb60
25. Fromentin C, Silva T, Dias TC, Morillo-Candas AS, Biondo O, Guaitella O, Guerra V (2023) Study of vibrational kinetics of CO_2 and CO in CO_2–O_2 plasmas under non-equilibrium conditions. Plasma Sources Sci Technol 32:024001. 10.1088/1361-6595/acb665
26. Petzold LR (1983) Automatic Selection of Methods for Solving Stiff and Nonstiff Systems of Ordinary Differential Equations. SIAM J Sci Stat Comput 4(1):136–148. 10.1137/0904010
27. Virtanen P, Gommers R, Oliphant TE, Haberland M, Reddy T, Cournapeau D et al (2020) SciPy 1.0: fundamental algorithms for scientific computing in Python. Nat Methods 17(3):261–272. 10.1038/s41592-019-0686-2
28. Van Laer K, Bogaerts A (2016) Fluid modelling of a packed bed dielectric barrier discharge plasma reactor. Plasma Sources Sci Technol 25:015002. 10.1088/0963-0252/25/1/015002
29. Van Laer K, Bogaerts A (2017) Influence of Gap Size and Dielectric Constant of the Packing Material on the Plasma Behaviour in a Packed Bed DBD Reactor: A Fluid Modelling Study. Plasma Process Polym 14:1600129. 10.1002/ppap.201600129
30. Van Laer K, Bogaerts A (2017) How bead size and dielectric constant affect the plasma behaviour in a packed bed plasma reactor: a modelling study. Plasma Sources Sci Technol 26:085007. 10.1088/1361-6595/aa7c59
31. Michielsen I, Uytdenhouwen Y, Pype J, Michielsen B, Mertens J, Reniers F, Meynen V, Bogaerts A (2017) CO_2 dissociation in a packed bed DBD reactor: first steps towards a better understanding of plasma catalysis. Chem Eng J 326:477–488. 10.1016/j.cej.2017.05.177
32. Wanten B, Maerivoet S, Vantomme C, Slaets J, Trenchev G, Bogaerts A (2022) Dry Reforming of Methane in an Atmospheric Pressure Glow Discharge: Confining the Plasma to Expand the Performance. J CO_2 Util 56:101869. 10.1016/j.jcou.2021.101869
33. .Kim XCH-H, Nozaki T (2024) Plasma catalytic technology for CH_4 and CO_2 conversion: A review highlighting fluidized-bed plasma reactor. Plasma Process Polym. 10.1002/ppap.202200207

34. Abbas T, Mohidin Yahya HS, Saidina Amin NA (2023) Non-thermal plasma catalytic dry reforming of methane over Ni-Co3O4 supported modified-titania catalysts: Effect of process conditions on syngas production, Fuel Process. Technol. 248, 107836 10.1016/j.fuproc.2023.107836
35. Kim J, Lim C, Lee D, Jeong H, Han JW, Ha K-S (2023) Effects of oxygen species in perovskite catalysts on the partial oxidation of methane in a low temperature plasma bed. J Catal 427:115116. 10.1016/j.jcat.2023.115116
36. Mei D, Shen X, Liu S, Zhou R, Yuan X, Rao Z, Sun Y, Fang Z, Du X, Zhou Y, Tu X (2023) Plasma-catalytic reforming of biogas into syngas over Ni-based bimetallic catalysts. Chem Eng J 462:142044. 10.1016/j.cej.2023.142044
37. Ahasan MR, Hossain MM, Barlow Z, Ding X, Wang R (2025) Dielectric Barrier Discharge Reactors for Plasma-Assisted CO_2 and CH_4 Conversion: A Comprehensive Review of Reactor Design, Performance, and Future Prospects. Energy Technol. 10.1002/ente.202401177
38. Ozkan A, Bogaerts A, Reniers F (2017) Routes to increase the conversion and the energy efficiency in the splitting of CO_2 by a dielectric barrier discharge. J Phys D: Appl Phys 50:084004. 10.1088/1361-6463/aa562c
39. Kozák T, Bogaerts A (2015) Evaluation of the energy efficiency of CO_2 conversion in microwave discharges using a reaction kinetics model. Plasma Sources Sci Technol 24:015024. 10.1088/0963-0252/24/1/015024
40. Berthelot A, Bogaerts A (2017) Modeling of CO_2 Splitting in a Microwave Plasma: How to Improve the Conversion and Energy Efficiency? J Phys Chem C 121(15):8236–8251. 10.1021/acs.jpcc.6b12840
41. Khunda D, Li S, Cherkasov N, Rishard MZM, Chaffee AL, Rebrov EV (2023) Effect of temperature on the CO_2 splitting rate in a DBD microreactor. React Chem Eng 8(9):2223–2233. 10.1039/D3RE00113J
42. Ullah S, Gao Y, Dou L, Liu Y, Shao T, Yang Y, Murphy AB (2023) Recent Trends in Plasma-Assisted CO_2 Methanation: A Critical Review of Recent Studies. Plasma Chem Plasma Process 43(6):1335–1383. 10.1007/s11090-023-10417-9
43. Sun J, Qu Z, Ostrikov K, Gao Y et al (eds) (2024) Plasma power-to-X (PP2X): status and opportunities for non-thermal plasma technologies, J. Phys. D: Appl. Phys. 57, 503002 10.1088/1361-6463/ad7bc4
44. Bogaerts A (2025) Plasma technology for the electrification of chemical reactions. Nat Chem Eng 2:336–340. 10.1038/s44286-025-00229-3
45. Biondo O, Wang K, Zhang H, Bogaerts A (2025) Coupling a CO_2 plasma with a carbon bed: the closer the better. Chem Eng J 507:160190. 10.1016/j.cej.2025.160190
46. O'Modhrain C, Gorbanev Y, Bogaerts A (2025) Post-plasma carbon bed design for CO_2 conversion: does size and insulation matter? J Energy Chem 104:312–323. 10.1016/j.jechem.2024.12.066

47. Vertongen R, Bogaerts A (2023) How important is reactor design for CO_2 conversion in warm plasmas? J CO_2 Util 72:102510. 10.1016/j.jcou.2023.102510
48. Bogaerts A, Neyts E (2018) Plasma Technology: An Emerging Technology for Energy Storage. ACS Energy Lett 3:1013–1027. 10.1021/acsenergylett.8b00184
49. Bogaerts A, Centi G (2020) Plasma Technology for CO_2 Conversion: A Personal Perspective on Prospects and Gaps. Front Energy Res 8:111. 10.3389/fenrg.2020.00111
50. Rouwenhorst KHR, Jardali F, Bogaerts A, Lefferts L (2021) From the Birkeland-Eyde process towards energy-efficient plasma-based NOx synthesis: a techno-economic analysis. Energy Environ Sci 14:2520–2534. 10.1039/D0EE03763J
51. Rouwenhorst KHR, Tabak S, Lefferts L (2024) Improving the energy yield of plasma-based NOx synthesis with in situ adsorption. React Chem Eng 9:528. 10.1039/D3RE00593C
52. Andersen J, Christensen J, Østberg M, Bogaerts A, Jensen A (2022) Plasma-catalytic ammonia decomposition using a packed-bed dielectric barrier discharge reactor. Int J Hydrogen Energy 47:32081–32091. 10.1016/j.ijhydene.2022.07.102
53. Meng S et al (2024) NH3 decomposition for H_2 production by thermal and plasma catalysis using bimetallic catalysts. Chem Eng Sci 283:119449. 10.1016/j.ces.2023.119449
54. Snoeckx R, Rabinovich A, Dobrynin D, Bogaerts A, Fridman A (2017) Plasma-Based Liquefaction of Methane: The Road from Hydrogen Production to Direct Methane Liquefaction. Plasma Process Polym 14:1600115. 10.1002/ppap.201600115
55. Ozkan A, Dufour T, Arnoult G, De Keyzer P, Bogaerts A, Reniers F (2015) CO_2-CH_4 conversion and syngas formation at atmospheric pressure using a multi-electrode dielectric barrier discharge. J CO_2 Util 9:74–81. 10.1016/j.jcou.2015.01.002
56. Troe J, Ushakov VG (2012) The dissociation/recombination reaction CH_4 (+ M) ⇔ CH_3 + H (+ M): a case study for unimolecular rate theory. J Chem Phys 136:214309. 10.1063/1.4717706
57. Fernandes RX, Luther K, Troe J, Ushakov VG (2008) The Temperature and Pressure Dependence of the Reactions H + O_2 (+ M) → HO_2 (+ M) and H + OH (+ M) → H_2O (+ M). J Phys Chem A 112:5085–5095. 10.1021/jp711800z
58. Baulch DL, Bowman CT, Cobos CJ, Cox RA, Just T, Kerr JA, Pilling MJ, Stocker D, Troe J, Tsang W, Walker RW, Warnatz J (2005) Evaluated Kinetic Data for Combustion Modeling: Supplement II. J Phys Chem Ref Data 34(3):757–1397. 10.1063/1.1748524
59. Orkin VL, Kozlov SN, Poskrebyshev GA, Kurylo MJ (2006) Rate Constant for the Reaction of OH with H_2 between 200 and 480 K. J Phys Chem A 110:6978–6985. 10.1021/jp057035b
60. Burkholder JB, Sander SP, Abbatt J, Barker JR, Huie RE, Kolb CE, Kurylo MJ, Orkin VL, Wilmouth DM, Wine PH (2015) Chemical Kinetics and Photochemical Data for Use in Atmospheric Studies, Evaluation No. 18. JPL Publication 15 – 10, Jet Propulsion Laboratory, Pasadena
61. Dean AM, Steiner DC (1977) A shock tube study of the recombination of carbon monoxide and oxygen atoms. J Chem Phys 66(2):598–604. 10.1063/1.433982

62. Tsang W, Hampson RF (1986) Chemical Kinetic Data Base for Combustion Chemistry. Part I. Methane and Related Compounds. J Phys Chem Ref Data 15(3):1087–1279. 10.1063/1.555759
63. Lo DY, Atreya SK, Wong MH, Trainer MG, Franz HB, McConnochie TH, Viúdez-Moreiras D, Mahaffy PR, Malespin CA (2024) Evaluating Atmospheric and Surface Drivers for O_2 Variations at Gale Crater as Observed by MSL SAM. Planet Sci J 5:65. 10.3847/PSJ/ad251b
64. Saidia L, Belasri A, Baadj S, Harrache Z (2019) Physico-Chemical Investigation of Pulsed Discharge in CO_2/O_2 Gas Mixture. Plasma Phys Rep 45(5):501–516. 10.1134/S1063780X1905009X
65. Khadir N, Khodja K, Belasri A (2017) Methane conversion using a dielectric barrier discharge reactor at atmospheric pressure for hydrogen production. Plasma Sci Technol 19(9):095502. 10.1088/2058-6272/aa6d6d

Figures

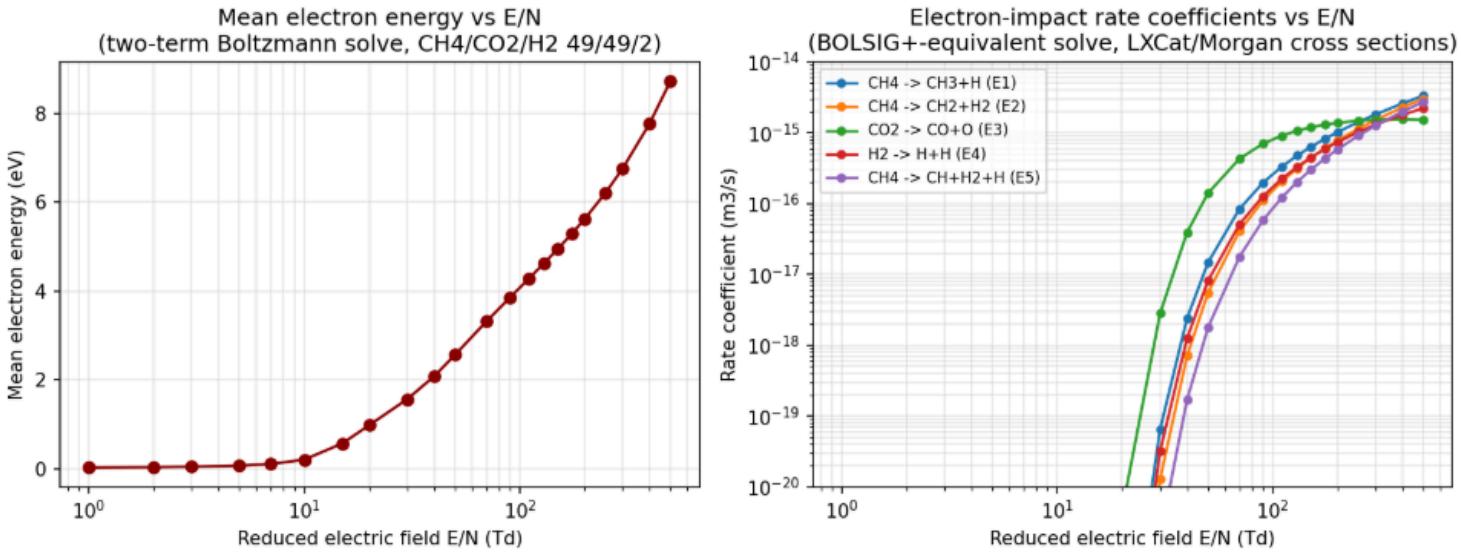


Figure 1

Mean electron energy (left) and electron-impact rate coefficients for reactions E1–E5 (right) as a function of the reduced electric field E/N, obtained by solving the electron Boltzmann equation (two-term approximation, BOLOS [19]) fed with LXCat/Morgan cross-sections [17] for a CH_4:CO_2:H_2 = 0.49:0.49:0.02 mixture.

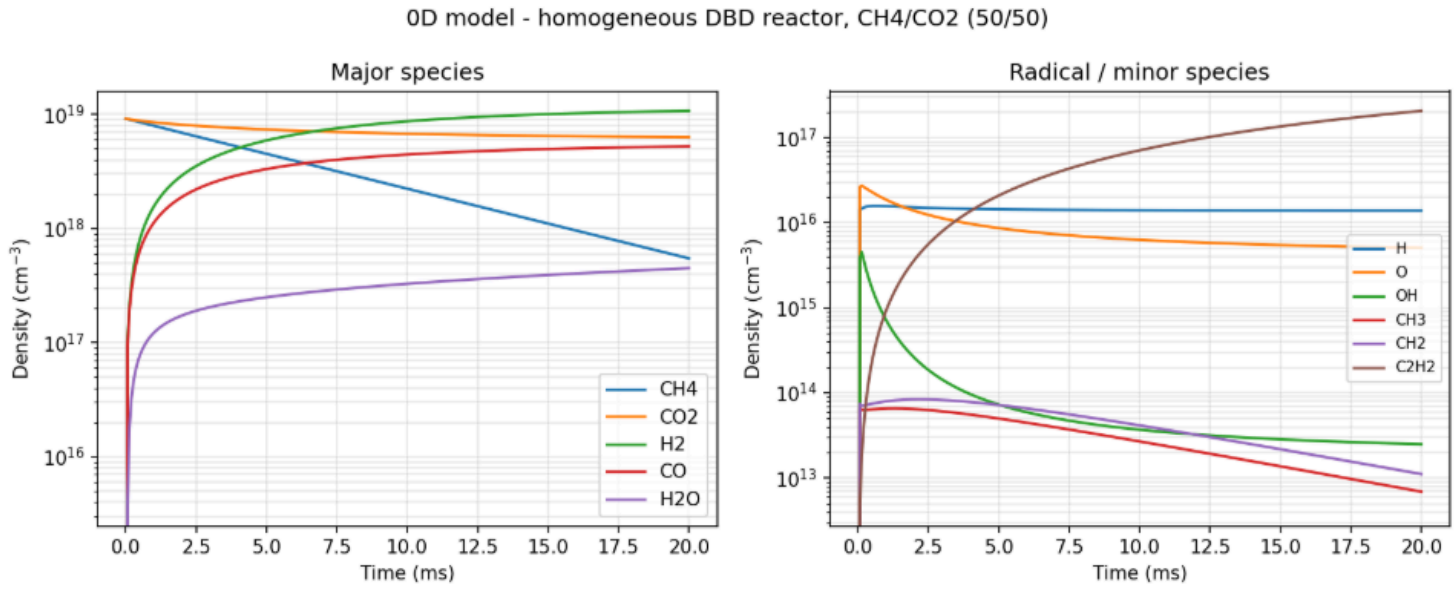


Figure 2

Time evolution of major-species (left) and radical/minor-species (right) number densities in the 0D model, for a 50/50 CH_4/CO_2 feed, a 20 ms residence time and the default plasma parameters (log scale).

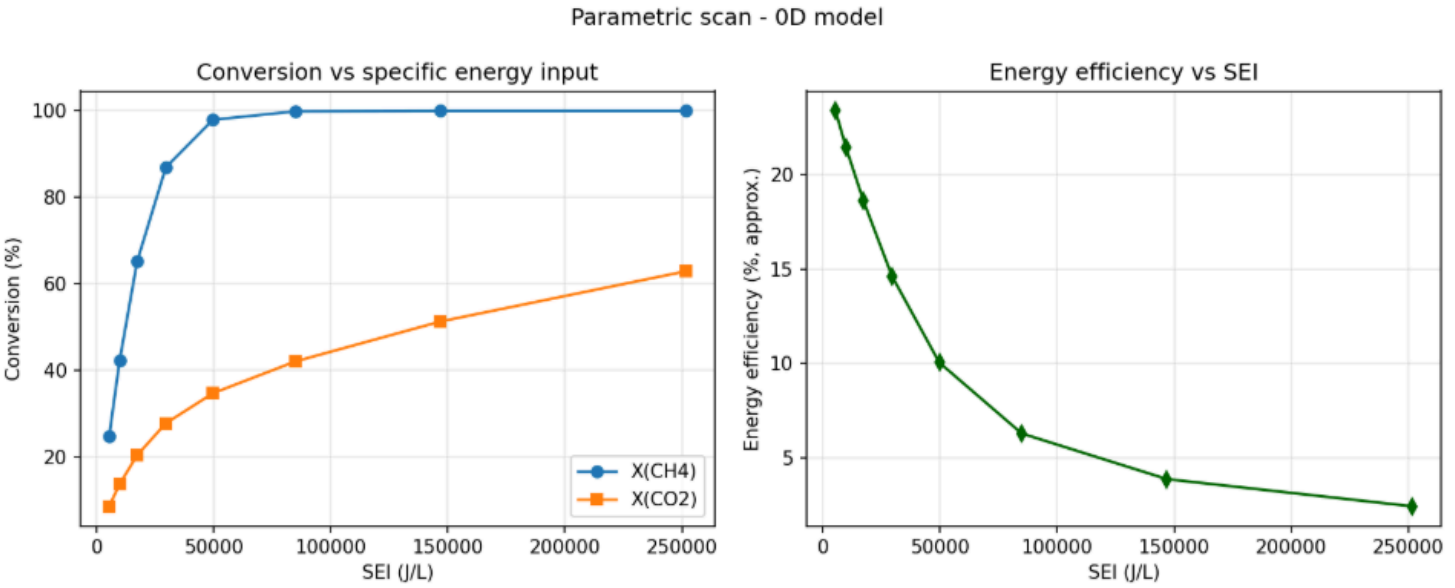


Figure 3

CH_4 and CO_2 conversion (left) and approximate energy efficiency (right) as a function of the specific energy input (SEI), obtained by scanning the peak electron density n_e,peak in the 0D model (t_res = 20 ms).

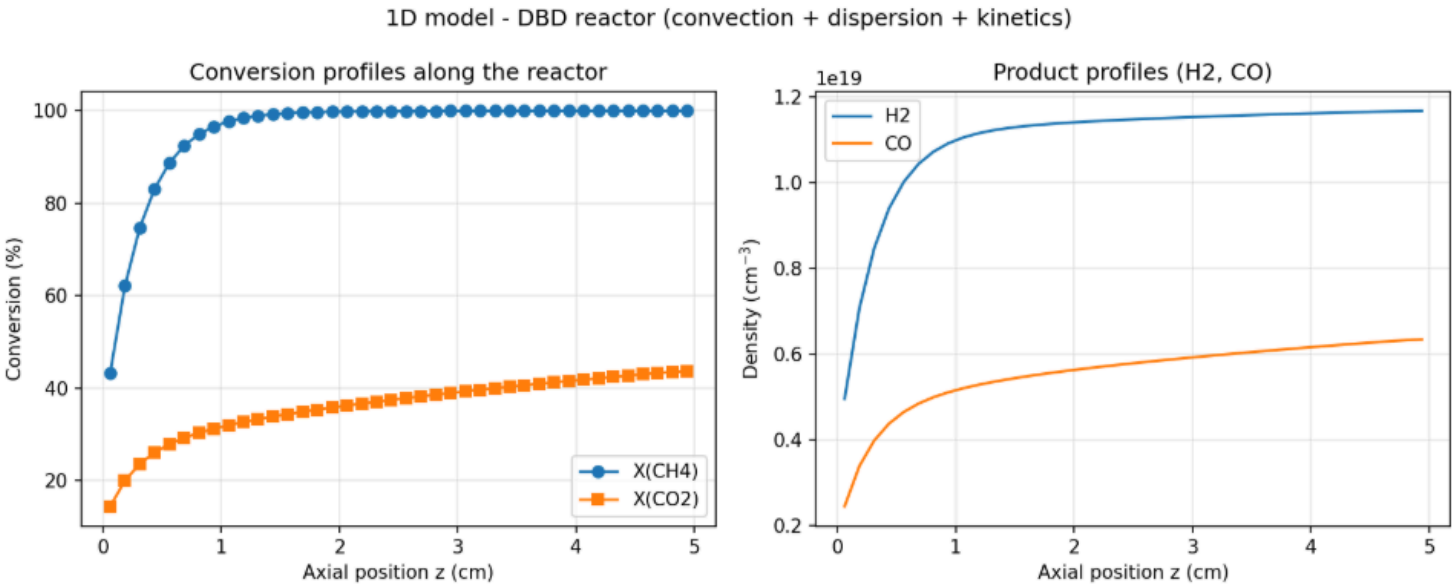


Figure 4

Axial profiles of CH_4 and CO_2 conversion (left) and of H_2 and CO number density (right) along the reactor (L = 5 cm, v = 0.3 m·s^{-1}, D_{ax} = 2×10^{-4} m^2·s^{-1}), 1D convection-dispersion-reaction model.

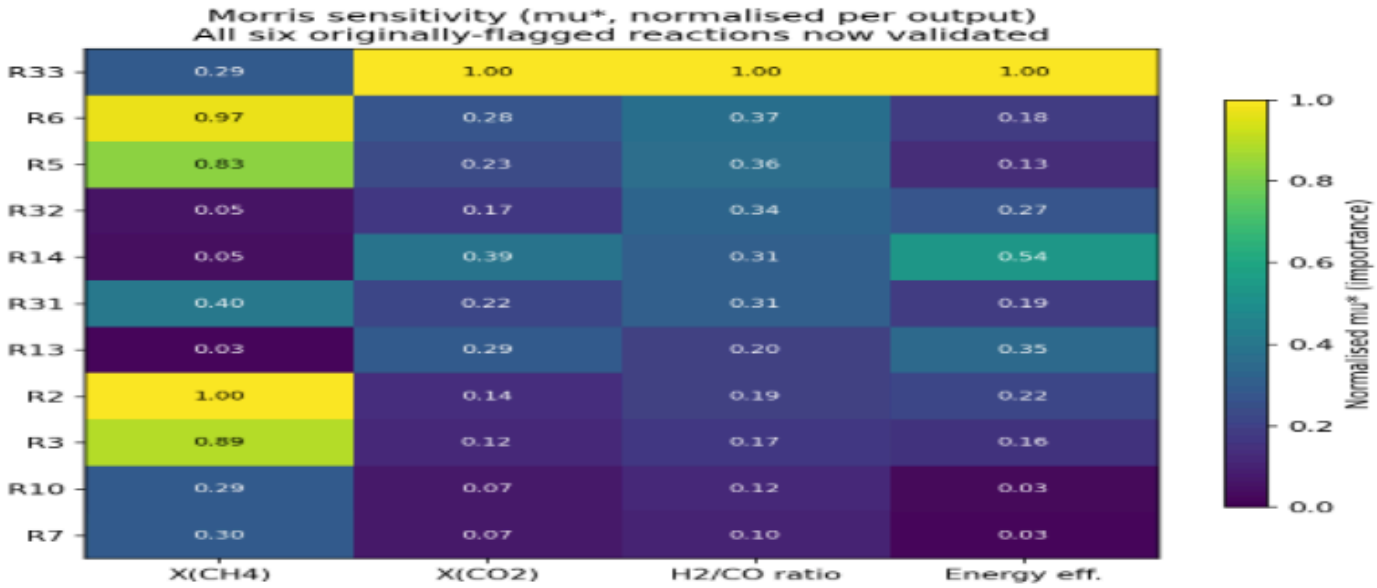


Figure 5

Morris sensitivity indices (μ, normalised to the maximum for each output), re-run after validating R2 and R11–R14 (Section 4.6), for the eleven rate constants (out of 33) that rank among the eight most influential for at least one output. Darker cells indicate a stronger influence of that rate constant on that output.*